Nanoscale

PAPER

View Article Online
View Journal | View Issue

Cite this: *Nanoscale*, 2016, **8**, 10774

Complete Au@ZnO core–shell nanoparticles with enhanced plasmonic absorption enabling significantly improved photocatalysis†

Yiqiang Sun,[a] Yugang Sun,*[b] Tao Zhang,[a] Guozhu Chen,[a] Fengshou Zhang,[a] Dilong Liu,[c] Weiping Cai,[c] Yue Li,*[c] Xianfeng Yang[d] and Cuncheng Li*[a]

Received 1st February 2016,
Accepted 23rd March 2016

DOI: 10.1039/c6nr00933f

www.rsc.org/nanoscale

Nanostructured ZnO exhibits high chemical stability and unique optical properties, representing a promising candidate among photocatalysts in the field of environmental remediation and solar energy conversion. However, ZnO only absorbs the UV light, which accounts for less than 5% of total solar irradiation, significantly limiting its applications. In this article, we report a facile and efficient approach to overcome the poor wettability between ZnO and Au by carefully modulating the surface charge density on Au nanoparticles (NPs), enabling rapid synthesis of Au@ZnO core–shell NPs at room temperature. The resulting Au@ZnO core–shell NPs exhibit a significantly enhanced plasmonic absorption in the visible range due to the Au NP cores. They also show a significantly improved photocatalytic performance in comparison with their single-component counterparts, *i.e.*, the Au NPs and ZnO NPs. Moreover, the high catalytic activity of the as-synthesized Au@ZnO core–shell NPs can be maintained even after many cycles of photocatalytic reaction. Our results shed light on the fact that the Au@ZnO core–shell NPs represent a promising class of candidates for applications in plasmonics, surface-enhanced spectroscopy, light harvest devices, solar energy conversion, and degradation of organic pollutants.

1. Introduction

Hybrid NPs with multiple components and a well-defined morphology represent an important class of materials that not only integrate different functions from distinct ingredients but also incubate new synergistic properties. Among them, metal–semiconductor hybrid NPs have attracted considerable attention because of their important applications in photocatalysis, solar energy conversion, and optoelectronics.[1–19] Tremendous efforts have been devoted to synthesizing semiconductor NPs decorated with small metal nanodomains, but rational synthesis of metal@semiconductor core–shell NPs still remains challenging. The metal core–semiconductor shell architecture not only effectively protects the metal core from corrosion, desquamation, and morphological changes, but also maximizes the active interfaces between the metal core and semiconductor shell through the three-dimensional contact to facilitate interfacial charge/energy transfer processes.[8–12] These advantages are beneficial for increasing the stability and the overall performance of the hybrid NPs.[20,21] Moreover, recent studies indicate that the plasmonic absorption of metal NPs could be distinctly enhanced if they are completely embedded into a semiconductor matrix.[8,22–24] As a result, the synthesis of metal@semiconductor core–shell NPs is a promising research topic in terms of both scientific and technological importance.[3,8–41]

Due to its chemical stability and unique optical-, mechanical-, and electronic-properties, ZnO has been intensively investigated for applications in UV-lasers,[42–44] piezoelectric generators,[45–47] solar cells,[48–50] and photocatalysis.[51–53] However, the wide band gap (3.37 eV) of ZnO makes pure ZnO NPs insensitive toward visible light, which significantly limits ZnO as an efficient photocatalyst. One promising solution is to form hybrid NPs with materials such as organic dyes,[48,49] narrow-gap semiconductor quantum dots,[54,55] or plasmonic metal NPs,[5–8] which can strongly absorb visible light to sensitize ZnO in the visible spectral range. On the other hand, these visible light sensitizers usually suffer degradation of the composition and the change of the morphology in practical appli-

[a]*School of Chemistry and Chemical Engineering, University of Jinan, Jinan 250022, Shandong, P. R. China. E-mail: chm_licc@ujn.edu.cn*
[b]*Department of Chemistry, Temple University, Philadelphia, Pennsylvania 19122, USA. E-mail: ygsun@temple.edu*
[c]*Key Laboratory of Material Physics, Anhui Key Lab of Nanomaterials and Nanotechnology, Institute of Solid State Physics, Chinese Academy of Sciences, Hefei 230031, Anhui, P. R. China. E-mail: yueli@issp.ac.cn*
[d]*Analytical and Testing Center, South China University of Technology, Guangzhou 510640, P. R. China*
†Electronic supplementary information (ESI) available. See DOI: 10.1039/c6nr00933f

cations since they are directly exposed to reactants and surrounding media. Therefore, the synthesis of Au@ZnO core–shell NPs with the plasmonic Au core completely encapsulated with the ZnO shell is expected to be an effective strategy for improving the stability and performance of ZnO-based photocatalysts although the synthesis is challenging.[26–31]

Herein, we report a facile and efficient approach for the synthesis of Au@ZnO core–shell NPs at room temperature by using octahedral Au NPs as an example to demonstrate the importance of the surface charge density on promoting deposition of ZnO on Au NPs. The resulting Au@ZnO core–shell NPs exhibit a significantly enhanced plasmonic absorption in the visible range and photocatalytic performance compared with their single-component counterparts, *i.e.*, the Au NPs and ZnO NPs. Such enhancements are attributed to the strong coupling between the Au core and the ZnO shell associated with their intimate contact, highlighting the promise of core–shell NPs in technological applications.

2. Experimental section

2.1 Synthesis of Au@ZnO core–shell NPs

For the synthesis of Au@ZnO core–shell NPs, octahedral Au NPs were firstly synthesized through a polyol process according to our previous work by using $HAuCl_4$ as the gold source and polydiallyldimethylammonium (PDDA) as a surfactant in an ethylene glycol solution.[56] Subsequently, 1.2 mL of 0.01 M aqueous $Zn(NO_3)_2$ (0.012 mmol) solution, 1.2 mL of 0.05 M aqueous NaOH (0.06 mmol) solution, and 0.6 ml of 0.02 M aqueous $NaBH_4$ (0.012 mmol) solution were added to 12 mL of Au octahedra colloidal solution in a plastic tube under ambient conditions. The final concentrations of $Zn(NO_3)_2$, NaOH, $NaBH_4$, and PDDA in the reaction solution were 0.8, 4.0, 0.8, and 20 mM, respectively. And then, the solution containing the Au octahedra and ZnO precursor was reacted at room temperature for 20 min. The color of the solution changed from red to blue, as displayed in Fig. 1 and S1.† Note that the dispersion of the mixed Au NPs and ZnO NPs appears red which is similar to that of pure Au NP colloidal solution since ZnO NPs do not exhibit any visible absorption. The as-synthesized Au@ZnO core–shell NPs were then collected *via* centrifugation at 14 500 rpm and the supernatant was discarded. The precipitated NPs were then washed with water and re-dispersed in water with the assistance of ultrasonication. The centrifugation and washing cycles were repeated two more times to remove the freestanding $NaBH_4$, NaOH, and PDDA. In the dispersion of washed Au@ZnO NPs, only a trace amount of PDDA adsorbed on the surface of the NPs exists. The dispersion of clean Au@ZnO core–shell NPs was then used for further characterization and photocatalysis study. After centrifugation, the blue products precipitated at the bottom of the tubes and the supernatant solution became clear and colorless, indicating that no residual products such as Au@ZnO, ZnO, or Au NPs existed in the solution. ZnO NPs were also synthesized at room temperature under static conditions following the procedure described above in the absence of octahedral Au NPs. Further experiments were conducted in order to determine the influence of reaction reagents on the synthesis of Au@ZnO core–shell NPs.

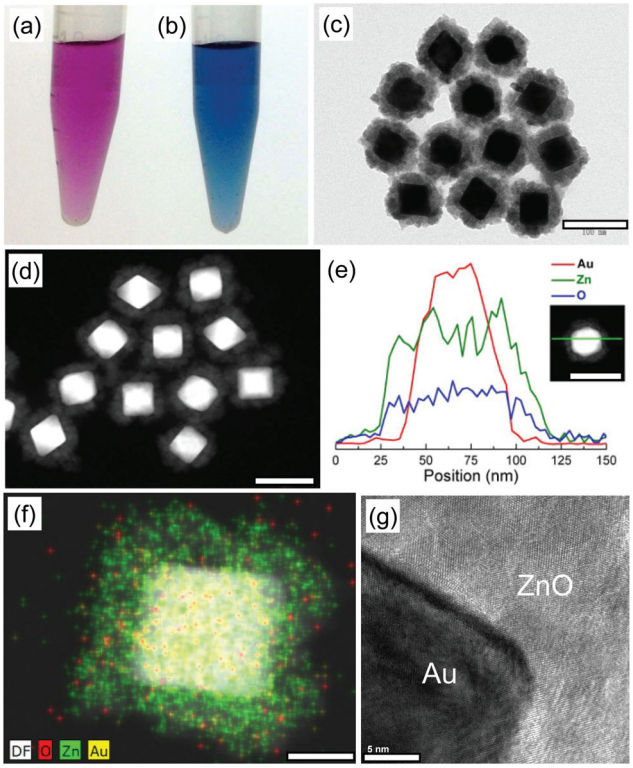

Fig. 1 Photographs of (a) Au octahedra and (b) the Au@ZnO core–shell NP colloidal solution; (c) TEM and (d) HAADF–STEM images of Au@ZnO core–shell NPs; (e) EDS line profile analysis of Au (red), Zn (green), and O (blue) elements on a single Au@ZnO core–shell NP; (f) elemental mapping of a single Au@ZnO core–shell NP; (g) HRTEM image recorded at the boundary of the Au core and ZnO shell. Scale bars for (c)–(e), (f), and (g) are 100 nm, 20 nm, and 5 nm, respectively.

2.2 Characterization

The products were characterized by transmission electron microscopy (TEM, JEM-1400), high-angle annular dark-field scanning TEM (HAADF-STEM), energy dispersive X-ray spectroscopy (EDS), and high-resolution TEM (HRTEM, JEM-2100F). X-ray diffraction (XRD) patterns were measured on a Bruker D8 Focus X-ray diffractometer with Cu Kα radiation (λ = 0.15418 nm) by depositing the product on a glass slide. The zeta potential of the dispersed Au NPs was recorded on a Zetasizer 3000HS analyzer (Malvern Instruments Ltd, Worcestershire, UK). For optical measurements, the optical extinction spectra were recorded with a Shimadzu UV-3101PC spectrophotometer.

2.3 Photocatalytic activity measurements

The photocatalytic activity of Au@ZnO core–shell NPs was measured by the degradation of the organic dye Rhodamine B (RhB), methyl orange (MO), and methyl blue (MB) in an

aqueous solution. Experiments by using pure ZnO NPs, Au NPs, and commercial P25-TiO_2 NPs as catalysts were also performed for comparison. For the photodegradation of RhB, the well-washed catalysts (8 mg, Au@ZnO core–shell NPs, ZnO NPs, or P25-TiO_2 NPs) were firstly added to 29.7 mL deionized water to form a suspension. And then, 0.3 mL of 1 mM aqueous organic dye (RhB, MO, or MB) solution was injected into the above suspension. The concentration of the organic dye in the initial suspension was 10^{-5} M. We recorded the adsorption kinetics of RhB on the surface of Au@ZnO core–shell NPs. The results indicated that 30 min is long enough to ensure that the adsorption/desorption equilibrium of the dye molecules on the surfaces of catalyst NPs can be reached (Fig. S2†). As estimated from the change of absorbance of RhB, ~7.8% RhB molecules were adsorbed on Au@ZnO core–shell NPs before the photocatalytic reaction was conducted. The photocatalytic test was conducted under irradiation with a 300 W xenon lamp at room temperature. The distance between the xenon lamp and the as-prepared suspension was about 10 cm. To measure the amount of the residue of RhB, a portion of the suspension irradiated for different times was sampled out during the photocatalytic experiments. The catalysts were first removed from the harvested suspension by centrifugation. After centrifugation, the catalyst precipitated at the bottom of the tubes. Subsequently, the supernatant solution was collected and diluted 15 times (×15) with deionized water for measuring the absorption of the organic dye on a spectrophotometer. The natural-sunlight-driven photocatalytic activity of Au@ZnO core–shell NPs was investigated through photodegradation of RhB under solar irradiation. To measure the visible light photocatalytic activity of catalysts, experiments were performed by introducing a UV filter in the path of the light beam to cut off the light below a wavelength of 420 nm.

Multi-cycle degradation experiments catalyzed by Au@ZnO core–shell NPs were conducted following a similar operation procedure described above. Briefly, the suspension containing Au@ZnO core–shell NPs and RhB was firstly irradiated for 10 min with a 300 W xenon lamp, then 2 mL of the suspension was taken out for measuring the degradation results of RhB, and finally a given amount of aqueous RhB solution was introduced into the remaining suspension for the recycled degradation experiment. Note that the concentration of RhB in the initial suspension was always kept at 10^{-5} M in the repeated degradation experiments. Meanwhile, the recovered precipitate (catalyst) was washed three times with water under sonicated for TEM observation.

3. Results and discussion

TEM and high-angle annular dark-field scanning TEM (HAADF-STEM) images show that the blue product is dominated by uniform core–shell NPs with rough surfaces (Fig. 1c and d). The core and shell in each NP exhibit significantly different image contrast, indicating that the core and shell are composed of different materials. The EDS analysis of an individual NP shows the distribution of Au, Zn, and O, *i.e.*, Au is located at the center of the NP while the Zn and O are detected in the shell (Fig. 1e). In addition, an elemental mapping image of a single NP further confirms that both Zn and O only exist in the shell (Fig. 1f). Note that each NP only contains a single core and particle with multiple cores or without cores is not found. The concentration of particles in the colloidal solution is thus unchanged after the formation of core–shell NPs except that the particle size increases. The HRTEM image shown in Fig. 1g highlights the core/shell interfaces, indicating that the shells are polycrystalline and consist of hexagonal-phase ZnO nanocrystallites with varying orientations. The uniform lattice fringes of the core agree well with face-centered cubic Au. These results indicate that each core–shell NP is composed of a single-crystalline Au core encapsulated with a polycrystalline ZnO shell. The diameter of the as-synthesized NPs is 100 ± 10 nm which is larger than the diagonal length (~60 nm) of the octahedral Au NPs (Fig. S3†). The dimensional difference indicates that the average thickness of the ZnO shell is ~20 nm. The corresponding XRD pattern further identifies that the as-obtained NPs are composed of Au (JCPDS 00-065-2870) and ZnO with a hexagonal wurtzite structure (JCPDS 00-065-3411), as presented in Fig. S4.† No peaks for Zn or other impurities are detected in the XRD pattern, indicating that the shell is pure ZnO. The XRD peaks from ZnO shells are very weak in contrast to that from the single-crystalline Au cores. This reflects that the shells were mainly composed of polycrystalline ZnO NPs with small grain sizes, which is in accordance with the HRTEM observation.

As presented in Fig. 1b, the colloidal solution of Au@ZnO core–shell NPs exhibits a blue color, which differs distinctly from that of the octahedral Au NPs (reddish), pure ZnO NPs (white), and a mixed solution of Au NPs and ZnO NPs (reddish) (Fig. S1†). This color difference indicates the formation of Au/ZnO intimate interfaces, which significantly influence the optical properties of Au NPs. Fig. 2 presents the

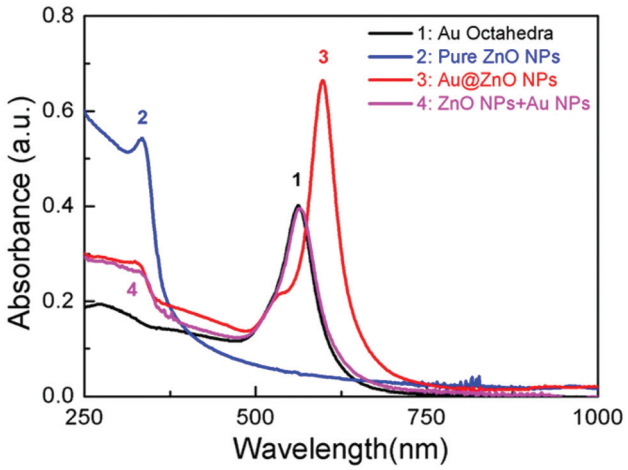

Fig. 2 Optical absorption spectra of (1) octahedral Au NPs, (2) ZnO NPs, (3) Au@ZnO core–shell NPs, and (4) the mixture of ZnO NPs and Au NPs quantitatively measured in an aqueous solution.

absorption spectra of the Au@ZnO core–shell NPs, octahedral Au NPs, the mixture of ZnO NPs and Au NPs, and pure ZnO NPs presented in Fig. S5.† The comparison clearly shows that the absorption spectrum of the Au@ZnO NPs is not the simple sum of that of the Au NPs and ZnO NPs. The formation of a ZnO shell around the Au core shifts the plasmonic absorption peak of the Au NPs from 560 nm to 600 nm due to the higher dielectric constant of ZnO than that of water.[15–17,23,42] It is worth noting that the absorption coefficient of the Au@ZnO core–shell NPs is significantly enhanced in comparison with that of Au NPs. Moreover, the absorption spectra and morphology of the as-prepared Au@ZnO NPs remain unchanged even after storage of their suspensions for several months under ambient conditions (Fig. S6†), indicating their excellent stability.

Since ZnO exhibits high chemical stability and reasonable photocatalytic activity in the UV spectral regime and the enhanced absorption coefficient of Au NPs in the visible regime associated with the formation of Au@ZnO core–shell structures, it makes the as-synthesized Au@ZnO core–shell NPs capable of efficiently driving photocatalysis with solar light. To illustrate this, a series of photocatalytic experiments were performed by using an organic dye as a probe and a 300 W xenon lamp as the simulated solar light source to evaluate the photocatalytic performance of Au@ZnO core–shell NPs. Fig. 3 compares the photocatalytic processes with the use of Au@ZnO core–shell NPs, pristine ZnO NPs, Au NPs, and commercial P25-TiO_2 NPs (Fig. S7,† TEM images of P25-TiO_2 NPs) for the degradation of organic dye RhB, indicating that Au@ZnO NPs act as a more efficient photocatalyst than ZnO NPs or TiO_2 NPs to degrade RhB (Fig. 3d). The degradation of RhB by using pure Au NPs as catalysts is consistent with the direct photoillumination of the RhB solution (without any NPs), indicating that pure Au NPs have no photocatalytic activity towards the degradation of organic dyes (Fig. 3d and S8†). The results indicate that Au@ZnO core–shell NPs are highly active for utilizing solar energy to degrade organic molecules. In addition, the Au@ZnO core–shell NPs can maintain their high catalytic activity even after 15 times of use (Fig. 3e). TEM observations indicate that the size and core–shell structure of the Au@ZnO NPs remained essentially unchanged after the photocatalytic reactions (Fig. S9†). The excellent photocatalytic activity of the Au@ZnO NPs is further confirmed by catalyzing the degradation of other organic dyes such as MO and MB (Fig. S10†). The degradation of RhB has also been realized by irradiating the aqueous solution of RhB and Au@ZnO NPs under natural sunlight (Fig. S11†), indicating that the as-synthesized Au@ZnO NPs are feasible to harvest natural solar energy to drive technologically important reactions.

In general, when a metal comes into contact with a semiconductor, an interfacial charge transfer occurs inevitably to achieve a Fermi level equilibration if their work functions are different. The work function of ZnO is about 4.45 eV, which is lower than that of Au (~5.31 eV).[59] Moreover, since the Fermi level of Au (E_F = 0.4 V *vs.* SHE) is more positive than the conduction band (CB) of ZnO (E_{CB} = −0.5 V *vs.* SHE),[60] it will be

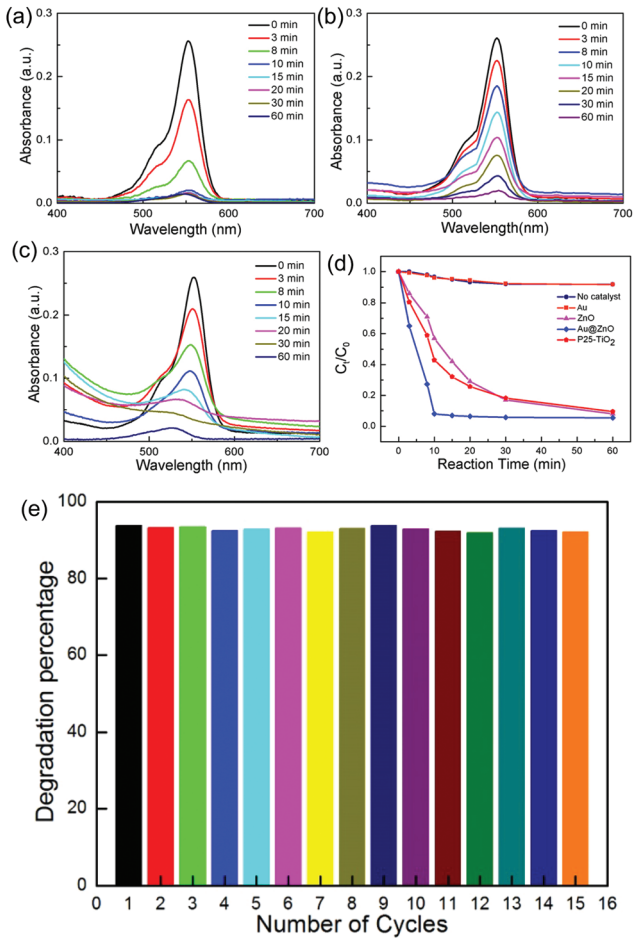

Fig. 3 UV-Vis spectral evolution of the aqueous RhB solution in the presence of (a) Au@ZnO core–shell NPs, (b) pristine ZnO NPs, and (c) commercial P25-TiO_2 NPs under irradiation with a 300 W xenon lamp at room temperature, (d) the photocatalytic performances (C_t/C_0) of Au@ZnO core–shell NPs, ZnO, P25-TiO_2, and Au octahedra for RhB, and (e) the multi-cycle degradation results of RhB catalyzed by Au@ZnO NPs.

facile for the electron transfer from ZnO to Au when they are in direct contact. Consequently, the Fermi level of Au shifts to a more negative potential until an equilibration with ZnO is achieved (the black dashed line in Fig. 4a). As is known, the increase of the electron density on the surfaces of Au NPs would lead to the enhancement of their plasmonic absorption. Our results clearly revealed that the surface plasmon resonance (SPR) of Au NPs was enhanced after the formation of the ZnO shell (see Fig. 2), directly suggesting that the electrons are transferred from ZnO to Au. Accordingly, the energy band of ZnO at the interface bends upward to form Schottky barriers and build-in electric field (red arrows in Fig. 4b) near the Au/ZnO interfaces, which can prevent the backward electron flow from ZnO to Au as well as facilitate the migration of holes from ZnO to Au.

Moreover, Au@ZnO core–shell NPs presented here exhibit remarkable absorption properties in the visible range. The photocatalytic activity of ZnO in the visible region was thus

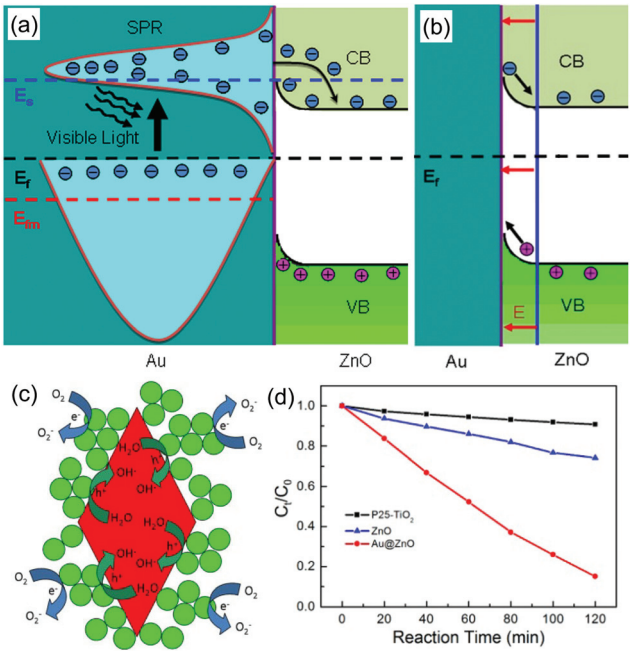

Fig. 4 (a) The proposed charge generation and transfer mechanism in Au@ZnO core–shell NPs under solar light irradiation. (b) Separation mechanism of photoexcited electrons and holes in or near the Schottky barriers formed in ZnO. The red arrows highlight the build-in electric field direction. (c) Photodegradation mechanism of active radicals over Au@ZnO core–shell NPs in a photodegradation reaction. (d) Photocatalytic activity of Au@ZnO, ZnO, and P25-TiO_2 NPs for RhB under visible light exposure.

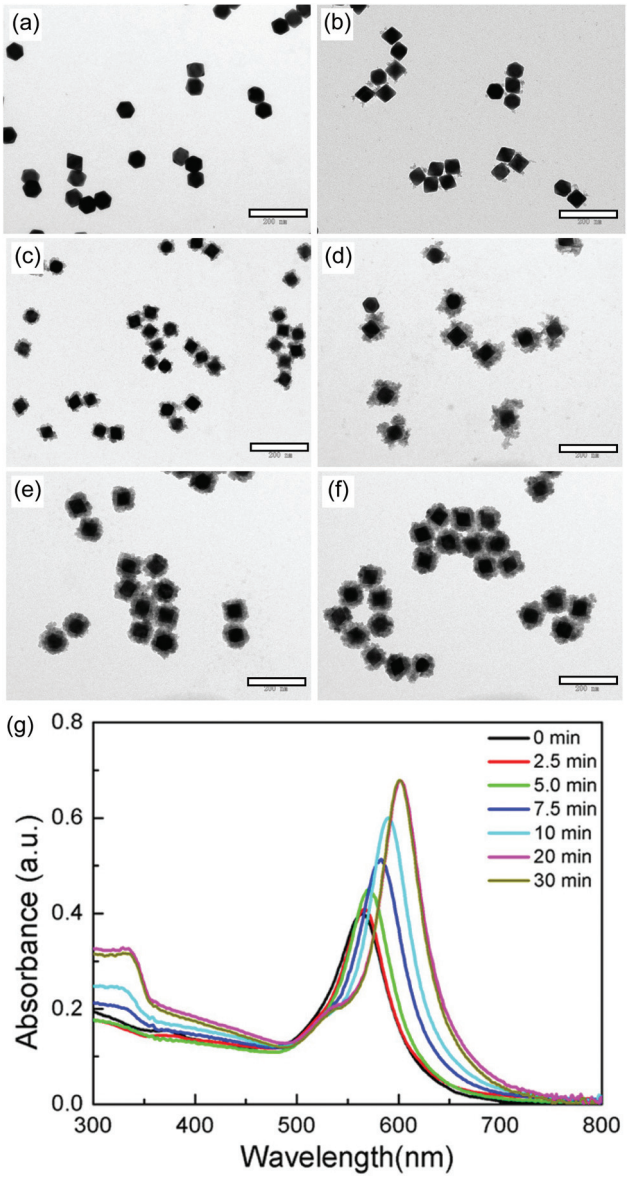

Fig. 5 TEM images of the products sampled in a one-pot reaction at (a) 2.5 min, (b) 5 min, (c) 7.5 min, (d) 10 min, (e) 20 min, and (f) 30 min, and (g) the corresponding UV-Vis-NIR spectra. Note that, for UV-Vis-NIR spectrum measurement, all the as-obtained reaction colloidal solutions were diluted fifteen times (×15) with water. All the scale bars are 200 nm.

triggered by the enhanced plasmonic absorption of Au cores. The energetic electrons are thus produced through the plasmonic excitation of Au cores when Au@ZnO core–shell NPs are exposed to visible light. If their energies are higher than the Schottky barriers (E_s, the blue dashed line in Fig. 4a), the energetic electrons can be facilely transferred from Au to the CB of ZnO through the black pathway as shown in Fig. 4a.[5–8,61] Subsequently, the energetic electrons are taken by the O_2 molecules adsorbed on the surfaces of ZnO NPs to produce superoxide radicals (Fig. 4c).[62] To verify the visible light photocatalytic activity of Au@ZnO core–shell NPs, experiments were further conducted by introducing a UV filter in the path of the light beam to cut off the light below a wavelength of 420 nm. The experimental results demonstrate that 84.5% RhB was degraded after visible light irradiation for 2 h in the presence of Au@ZnO core–shell NPs. The corresponding degradation of RhB was only 26.2% and 9.2% by using pristine ZnO NPs and P25-TiO_2 NPs as catalysts (Fig. S12†). Apparently, among them, Au@ZnO core–shell NPs are ideal candidates for visible light active photocatalysis because of their remarkable plasmonic absorption. On the basis of our results and the above discussions, it is reasonable to conclude that the synergic effect between the Au core and ZnO shell is responsible for the higher degradation efficiency of Au@ZnO core–shell NPs under solar irradiation. It is because that (i) the formation of Schottky barriers enhances the separation of the photoexcited electron–hole pairs when the ZnO is excited under solar irradiation, and (ii) the photocatalytic activity of ZnO in the visible range is triggered by the outstanding plasmonic absorption of Au NPs.

The formation process of Au@ZnO core–shell NPs was investigated by TEM observation and optical measurement. TEM images of the products sampled at different times in a one-pot reaction are shown in Fig. 5. Our results revealed that ZnO starts to be adsorbed on the surfaces of Au NPs at 5 min of the reaction and the thickness of ZnO shells gradually increases to a maximum of ~20 nm at a reaction time longer

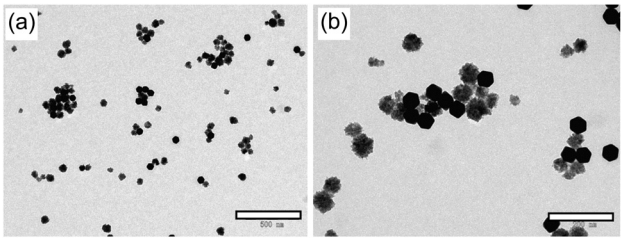

Fig. 6 (a) Low and (b) high magnification TEM images of the sample synthesized at room temperature with 0.8 mM $Zn(NO_3)_2$, 4.0 mM NaOH, and 20 mM PDDA but in the absence of $NaBH_4$ (0 mM). Scale bars for (a) and (b) are 500 nm and 200 nm, respectively.

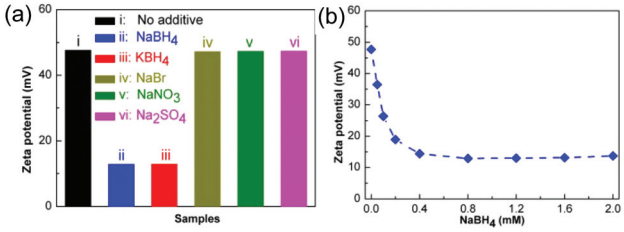

Fig. 7 (a) Zeta-potential of (i) the as-synthesized Au octahedra and (ii–vi) Au octahedra mixed with 0.8 mM of (ii) $NaBH_4$, (iii) KBH_4, (iv) NaBr, (v) $NaNO_3$, (vi) Na_2SO_4; (b) The evolution of the zeta-potential of Au octahedra along with $NaBH_4$ concentrations from 0 to 2.0 mM.

than 20 min. The gradual growth of ZnO shell leads to a monotonically red-shift and enhancement of the absorption peak of the Au NPs (Fig. 5g). As aforementioned, the color of the reacted solution changes from reddish to blue because of the change in the dielectric environment around Au NPs (Fig. 1b).[22–24,32,57]

A series of experiments have been performed to investigate the influences of different experimental parameters involved in the formation of Au@ZnO core–shell NPs. First, $NaBH_4$ is important for the success in forming the ZnO shells out of the Au NPs. Fig. 6 shows the TEM images of the product NPs synthesized without using $NaBH_4$. TEM observation indicates that the harvested product is a mixture of octahedral Au NPs and 20–50 nm ZnO NPs. No Au@ZnO core–shell NPs are observed in this case. The results indicate that ZnO prefers self-nucleation to form ZnO NPs rather than heterogeneous growth on the surfaces of Au NPs in the absence of $NaBH_4$, highlighting the importance of $NaBH_4$ in the selective deposition of ZnO on the surfaces of Au NPs to form Au@ZnO core–shell NPs.

Our previous work revealed that PDDA molecules were strongly adsorbed on the surface of Au octahedra harvested by the PDDA-mediated polyol process.[56] PDDA is known to be a cationic polyelectrolyte. The Au NPs coated with $[PDDA]^+$ cations thus exhibit a highly positive zeta potential (47.72 mV, Fig. 7a) that may prevent ZnO from being adsorbed on the surfaces of the Au NPs. Interestingly, a recent study indicated that H^- anions have higher binding affinity to Au than other molecules.[58] Surfactants can be readily stripped from the Au surfaces by H^- anions released from BH_4^- ions. Stripping PDDA from Au NPs will result in the decrease of the density of positive charges on their surfaces. To verify our claim, the zeta potential of Au NPs mixed with 0.8 mM of various salts, *e.g.*, $NaBH_4$, KBH_4, NaBr, $NaNO_3$, and Na_2SO_4, was measured using a zeta potential analyzer. Our results clearly illustrated that the zeta potential of the Au NPs was greatly decreased in the presence of borohydride and almost unchanged in the other cases (Fig. 7a). This comparison further confirms that only H^- anions released from BH_4^- ions are capable of reducing the charge density of the Au NPs. Further experiments were carried out to investigate the evolution of the zeta potential of octahedral Au NPs along with the concentration of $NaBH_4$, as illustrated in Fig. 7b. The positive zeta potential of the Au NPs

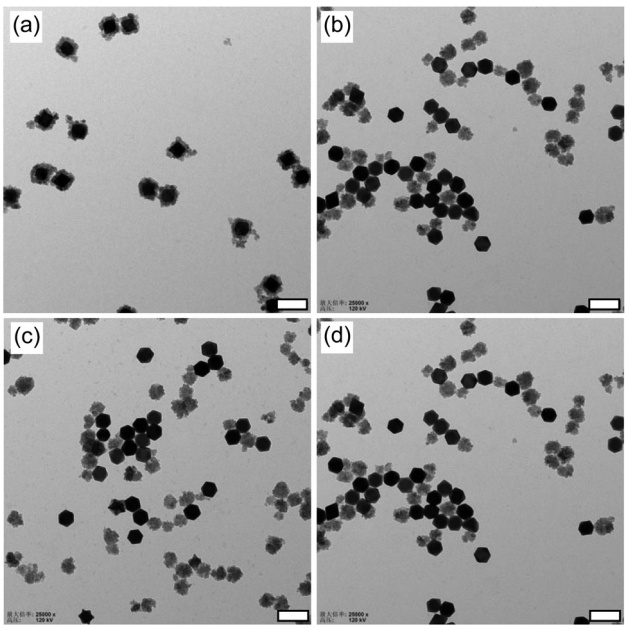

Fig. 8 TEM images of the sample synthesized at room temperature by using (a) KBH_4, (b) NaBr, (c) $NaNO_3$, and (d) Na_2SO_4 instead of $NaBH_4$. All scale bars are 100 nm.

gradually decreases if the $NaBH_4$ concentration is increased from 0 to 0.4 mM. When the concentration of $NaBH_4$ is higher than 0.4 mM, the zeta potential of Au NPs will maintain a constant value (~12.88 mV), reflecting that the replacement of $[PDDA]^+$ cations with H^- anions to form chemical bonding with Au atoms of the particle surface reaches an equilibrium.

Based on the above zeta potential analyses, a series of synthetic experiments were designed to further illustrate the effect of zeta potential for the synthesis of Au@ZnO core–shell NPs. Our results indicated that Au@ZnO core–shell NPs were readily produced when KBH_4 was used as a $NaBH_4$ substitute (Fig. 8a), whereas the final products were a mixture of isolated ZnO NPs and bare Au octahedra by using NaBr, $NaNO_3$, or Na_2SO_4 instead of $NaBH_4$ (Fig. 8b–d). Moreover, we found that (i) high-yield Au@ZnO core–shell NPs were formed only when the reaction solutions contained $NaBH_4$ with a concentration ≥0.2 mM (Fig. 9) and (ii) no Au@ZnO core–shell NPs were pro-

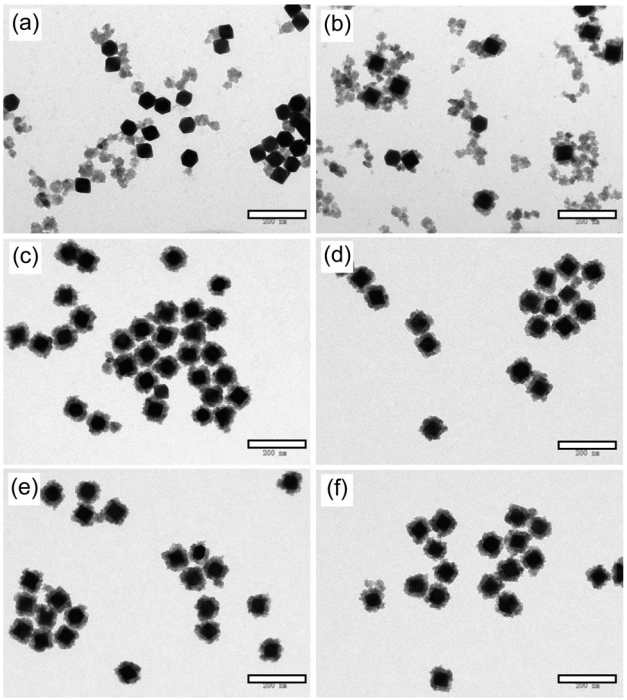

Fig. 9 TEM images of the products synthesized in the presence of $NaBH_4$ with various concentrations: (a) 0.1 mM; (b) 0.15 mM; (c) 0.2 mM; (d) 0.4 mM; (e) 1.2 mM; (f) 2.0 mM. The result without using $NaBH_4$ is presented in Fig. 6. All scale bars are 200 nm.

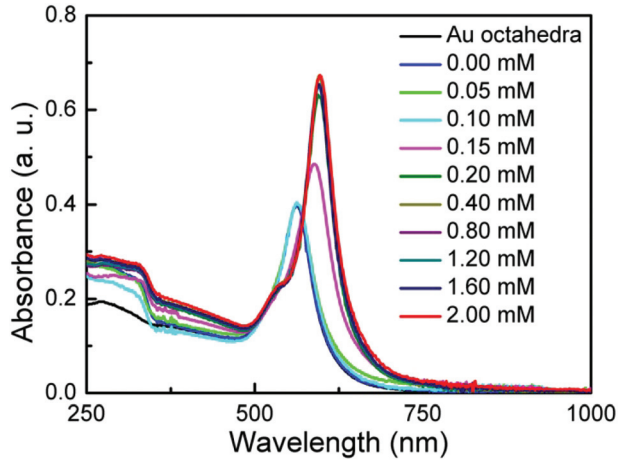

Fig. 10 UV-Vis-NIR spectra of the products obtained by using $NaBH_4$ with a concentration range from 0 to 2.0 mM and octahedral Au NPs. The corresponding TEM images are presented in Fig. 6, 9, and S13.†

duced when the concentration of borohydride was lower than 0.1 mM even if the reaction time was increased to 24 h (Fig. 9a and S13†). This is consistent with the optical measurements as displayed in Fig. 10. The optical absorption spectra of the samples synthesized by using $NaBH_4$ concentrations higher than 0.2 mM are essentially identical, reflecting that the identical products are yielded (Fig. 6c–f). As aforementioned, the zeta potential of Au octahedra is lower than 18.92 mV at $[NaBH_4]$ ≥0.2 mM (see Fig. 7b), whereas, for the samples (Fig. 6, 9a, and S13†) obtained by using $NaBH_4$ with a concentration lower than 0.1 mM (corresponding zeta potential ≥26.38 mV), besides the ground exciton absorption band of ZnO NPs in the UV region, the corresponding optical absorption spectra are the same as that of octahedral Au seeds: the plasmonic absorption of the samples has no increment or shift compared with that of the original Au octahedra. This indicates that there is no interaction between Au octahedra and the as-formed ZnO NPs. The results described above clearly demonstrate that lowering the zeta potential of Au NPs by introducing borohydride into the reaction solution is critical for the successful synthesis of Au@ZnO core–shell NPs.

Besides $NaBH_4$, other reaction parameters including the concentration of PDDA and NaOH in the reaction solution as well as the reaction temperature were also systematically investigated in our experiments. As shown in Fig. S14,† only octahedral Au NPs were observed in the final product when the NaOH concentration was lower than 0.4 mM (Fig. S14a–d†). No Au@ZnO or ZnO NPs were produced even by using $NaBH_4$ with a high concentration such as 15 mM (Fig. S14d†). This indicates that NaOH with a concentration higher than 0.4 mM is necessary for the fabrication of Au@ZnO core–shell NPs. Actually, in the present experiments, the formation of ZnO relies on the decomposition of $Zn(OH)_2$ or $Zn(OH)_4^{2-}$, which is formed through a reaction between Zn^{2+} ions (from $Zn(NO_3)_2$) and OH^- ions (from NaOH). As illustrated in the Experimental section, the ZnO precursor was directly introduced into the as-obtained Au octahedral colloid for the fabrication of Au@ZnO NPs and no purification was carried out. H^+ ions (~0.4 mM) released from $HAuCl_4$ are thus existed in the reaction system because they are not consumed during the formation process of Au octahedra. The neutral reaction between H^+ and OH^- ions unavoidably occurred. Therefore, Au@ZnO or ZnO NPs were not yielded when the concentration of NaOH was lower than 0.4 mM. Experiments by keeping $Zn(NO_3)_2$ at 0.8 mM in the reaction system illustrate that Au@ZnO NPs were predominately synthesized when the NaOH concentration was higher than 0.8 mM (Fig. S14e–l†). Moreover, we found that (i) ZnO NPs on the surfaces of Au octahedra were gradually increased when the NaOH concentration was increased from 0.8 to 2.0 mM (Fig. S14e–g†) and (ii) Au@ZnO core–shell NPs with identical ZnO shell thicknesses were harvested when the NaOH concentration was higher than 2.0 mM (Fig. S14h–l†). These results indicate that the molar ratio of OH^-/Zn^{2+} ions in the reaction solution must be higher than 2 to convert the entire Zn source into ZnO.

Further experiments were performed by changing the concentration of PDDA in the reaction precursors and keeping all the other parameters identical to the case of Fig. 1. Our results indicated that the product obtained with a reaction time of 20 min was composed of ZnO NPs and Au NPs in the absence of PDDA (Fig. S15a†). In this case, octahedral Au seeds were firstly well-washed with water to remove the surfactant PDDA in the reaction system. Interestingly, with a reaction time of 10 h, ZnO NPs disappeared and the final product was

dominated by Au@ZnO core–shell NPs (Fig. S15b†). Further experiments indicate that Au@ZnO core–shell NPs were predominately harvested with a reaction time of 20 min when the PDDA concentration was in the range of 5 to 35 mM (Fig. S15c–e†). However, the product was made up of Au@ZnO core–shell NPs together with ZnO NPs as the PDDA concentration was higher than 50 mM (Fig. S15f–h†). Apparently, surfactant PDDA with an optimal concentration (5–35 mM) is very important for rapid fabrication of high-quality Au@ZnO core–shell NPs. As the experimental description, surfactant PDDA has been existed in the as-synthesized octahedral Au NP colloidal solution. Therefore, in the standard synthesis process for Au@ZnO core–shell NPs, besides the ZnO precursor, we do not introduce additional PDDA into the reaction system.

Generally, the reaction temperature greatly affects the decomposition rate of $(Zn(OH)_2)$ or $Zn(OH)_4^{2-}$ ions, which alters the degree of supersaturation of ZnO, and hence the nucleation and growth of ZnO NPs. Experiments under different reaction temperatures were conducted. It was observed that the duration of the color change became shortened upon increasing the reaction temperature. For example, the color of the reaction solution changed from reddish to blue after being heated for about 6 min at 100 °C. On the contrary, when the experiment was carried out at 0 °C, no color change was observed during the initial 20 min. With a reaction time of 45 min, the color of the solution appears blue, reflecting the formation of Au@ZnO core–shell NPs. This is consistent with the optical measurements and TEM observations displayed in Fig. S16 and S17.† Our results showed that (i) the formation rate of Au@ZnO core–shell NPs was kinetically enhanced at a high temperature and (ii) Au@ZnO core–shell NPs could be dominantly produced over a broad temperature range (0 to 100 °C). Consequently, the method presented here is a reliable and effective synthetic strategy for Au@ZnO core–shell NPs. Moreover, it is also a time- and energy-efficient route because Au@ZnO core–shell NPs can be readily and successfully produced at room temperature within tens of minutes.

4. Conclusions

In conclusion, we have developed a facile and efficient strategy for rapid synthesis of uniform Au@ZnO core–shell NPs at room temperature by carefully tuning the surface charge density on the Au NPs. The role of specific experimental parameters including $NaBH_4$, NaOH, PDDA, and the reaction temperature involved in the formation of Au@ZnO core–shell NPs have been systematically investigated and identified. The surface charge density on the Au NPs represents the most determining parameter for the success in forming Au@ZnO core–shell NPs. Most importantly, the formation of complete ZnO shells on the Au NPs significantly enhances the plasmonic absorption of the Au NPs, in particular in the visible spectral region, resulting in a significant enhancement in the photocatalytic performance of the resultant Au@ZnO core–shell NPs. Their high catalytic activity can be maintained even after many cycles of photocatalytic reaction because of the essentially unchanged size and morphology of the Au@ZnO NPs. The as-synthesized Au@ZnO core–shell NPs with remarkable optical properties and excellent stability are one of the promising candidates for application in surface plasmonics, nanophotonics, surface-enhanced spectroscopy, light harvest devices, solar energy conversion, and degradation of organic pollutants.

Acknowledgements

This work was financially supported by the National Natural Science Foundation of China (Grant No. 21103068 and 51371165), the National Basic Research Program of China (Grant No. 2012CB932303), the Cross-disciplinary Collaborative Teams and CAS/SAFEA International Partnership Program for Creative Research Teams, and the Shandong Provincial Natural Science Foundation, China (Grant no. ZR2015BM008). C. C. Li as a Taishan Scholar Endowed Professor acknowledges the support from the Shandong province and UJN. Y. Li acknowledges the Recruitment Program of Global Experts (C). Y. Sun thanks the startup support from Temple University.

References

1 S. K. Cushing, J. T. Li, F. K. Meng, T. R. Sentry, S. Suri, M. J. Zhi, M. Li, A. D. Bristow and N. Q. Wu, *J. Am. Chem. Soc.*, 2012, **134**, 15033–15041.
2 S. T. Kochuveedu, Y. H. Jang and D. H. Kim, *Chem. Soc. Rev.*, 2013, **42**, 8467–8493.
3 R. B. Jiang, B. X. Li, C. H. Fang and J. F. Wang, *Adv. Mater.*, 2014, **26**, 5274–5309.
4 I. Concina and A. Vomiero, *Small*, 2015, **11**, 1744–1774.
5 P. Li, Z. Wei, T. Wu, Q. Peng and Y. D. Li, *J. Am. Chem. Soc.*, 2011, **133**, 5660–5663.
6 J. Lee, H. S. Shim, M. Lee, J. K. Song and D. Lee, *J. Phys. Chem. Lett.*, 2011, **2**, 2840–2845.
7 H. M. Chen, C. K. Chen, C. J. Chen, L. C. Cheng, P. C. Wu, B. H. Cheng, Y. Z. Ho, M. L. Tseng, Y. Y. Hsu, T. S. Chan, J. F. Lee, R. S. Liu and D. P. Tsai, *ACS Nano*, 2012, **6**, 7362–7372.
8 C. Chen, Y. F. Lu, H. P. He, K. W. Wu and Z. Z. Ye, *Appl. Phys. A*, 2013, **110**, 47–53.
9 J. S. Lee, E. V. Shevchenko and D. V. Talapin, *J. Am. Chem. Soc.*, 2008, **130**, 9673–9675.
10 Z. H. Sun, Z. Yang, J. H. Zhou, M. H. Yeung, W. H. Ni, H. K. Wu and J. F. Wang, *Angew. Chem., Int. Ed.*, 2009, **48**, 2881–2885.
11 J. Zhang, Y. Tang, K. Lee and M. Ouyang, *Science*, 2010, **327**, 1634–1638.

12 F. Nan, S. Liang, J. H. Wang, X. L. Liu, D. J. Yang, X. F. Yu, L. Zhou, Z. H. Hao and Q. Q. Wang, *Adv. Opt. Mater.*, 2014, **2**, 679–686.
13 C. H. Fang, H. L. Jia, S. Chang, Q. F. Ruan, P. Wang, T. Chen and J. F. Wang, *Energy Environ. Sci.*, 2014, **7**, 3431–3438.
14 J. Zhao, M. D. Xiao, Z. H. Bao, P. Wang and J. F. Wang, *Angew. Chem., Int. Ed.*, 2012, **51**, 6406–6410.
15 J. Yin, C. Yue, Y. S. Zang, C. H. Chiu, J. C. Li, H. C. Kuo, Z. H. Wu, J. Li, Y. Y. Fang and C. Q. Chen, *Nanoscale*, 2013, **5**, 4436–4442.
16 C. L. Yu, K. Yang, Y. Xie, Q. Z. Fan, J. C. Jimmy, Q. Shu and C. Y. Wang, *Nanoscale*, 2013, **5**, 2142–2151.
17 F. Kayaci, S. Vempati, C. O. Akgun, I. Donmez, N. Biyikli and T. Uyar, *Nanoscale*, 2014, **6**, 5735–5745.
18 S. Pal, S. Maiti, U. N. Maiti and K. K. Chattopadhyay, *CrystEngComm*, 2015, **17**, 1464–1476.
19 L. Zhang, H. Z. Li, Y. Liu, Z. Tian, B. Yang, Z. B. Sun and S. Q. Yan, *RSC Adv.*, 2014, **4**, 48703–48711.
20 J. T. Li, S. K. Cushing, J. Bright, F. K. Meng, T. R. Senty, P. Zheng, A. D. Bristow and N. Q. Wu, *ACS Catal.*, 2013, **3**, 47–51.
21 L. Ma, S. Liang, X. L. Liu, D. J. Yang, L. Zhou and Q. Q. Wang, *Adv. Funct. Mater.*, 2015, **25**, 898–904.
22 L. Zhang, D. A. Blom and H. Wang, *Chem. Mater.*, 2011, **23**, 4587–4598.
23 D. Y. Liu, S. Y. Ding, H. X. Lin, B. J. Liu, Z. Z. Ye, F. R. Fan, B. Ren and Z. Q. Tian, *J. Phys. Chem. C*, 2012, **116**, 4477–4483.
24 L. Zhang, H. Jing, G. Boisvert, J. Z. He and H. Wang, *ACS Nano*, 2012, **6**, 3514–3527.
25 C. H. Kuo, T. E. Hua and M. H. Huang, *J. Am. Chem. Soc.*, 2009, **131**, 17871–17878.
26 W. C. Wang, L. M. Lyu and M. H. Huang, *Chem. Mater.*, 2011, **23**, 2677–2684.
27 L. N. Kong, W. Chen, D. K. Ma, Y. Yang, S. S. Liu and S. M. Huang, *J. Mater. Chem.*, 2012, **22**, 719–724.
28 Y. C. Yang, H. J. Wang, J. Whang, J. Huang, L. M. Lyu, P. H. Lin, S. Gwo and M. H. Huang, *Nanoscale*, 2014, **6**, 4316–4324.
29 M. E. Aguirre, H. B. Rodriguez, E. S. Roman, A. Feldhoff and M. A. Grela, *J. Phys. Chem. C*, 2011, **115**, 24967–24974.
30 T. T. Jiang, X. Y. Qin, Y. Sun and M. Yu, *RSC Adv.*, 2015, **5**, 65595–65599.
31 O. K. Ranasingha, C. J. Wang, P. R. O. Jr., J. W. Lekse, J. P. Lewis and C. Matranga, *J. Mater. Chem. A*, 2015, **3**, 15141–15147.
32 Y. Z. Chen, D. Q. Zeng, M. B. Cortie, A. Dowd, H. Z. Guo, J. B. Wang and D. L. Peng, *Small*, 2015, **11**, 1460–1469.
33 H. Jing, N. Large, Q. F. Zhang and H. Wang, *J. Phys. Chem. C*, 2014, **118**, 19948–19963.
34 H. Sun, J. T. He, J. Y. Wang, S. Y. Zhang, C. C. Liu, T. Sritharan, S. Mhaisalkar, M. Y. Han, D. Wang and H. Y. Chen, *J. Am. Chem. Soc.*, 2013, **135**, 9099–9110.
35 Y. Yang, S. H. Han, G. J. Zhou, L. J. Zhang, X. L. Li, C. Zou and S. M. Huang, *Nanoscale*, 2013, **5**, 11808–11819.
36 S. M. Majhi, P. Rai and Y. T. Yu, *ACS Appl. Mater. Interfaces*, 2015, **7**, 9462–9468.
37 J. Qi, J. Chen, G. D. Li, S. X. Li, Y. Gao and Z. Y. Tang, *Energy Environ. Sci.*, 2012, **5**, 8937–8941.
38 W. L. Liu, F. C. Lin, Y. C. Yang, C. H. Huang, S. Gwo, M. H. Huang and J. S. Huang, *Nanoscale*, 2013, **5**, 7953–7962.
39 B. X. Li, T. Gu, T. Ming, J. X. Wang, P. Wang, J. F. Wang and J. C. Yu, *ACS Nano*, 2014, **8**, 8152–8162.
40 H. Y. Zhu, A. Sigdel, S. Zhang, D. Su, Z. Xi, Q. Li and S. H. Sun, *Angew. Chem., Int. Ed.*, 2014, **53**, 12508–12512.
41 N. Zhang, S. Q. Liu, X. Z. Fu and Y. J. Xu, *J. Phys. Chem. C*, 2011, **115**, 9136–9145.
42 M. H. Huang, S. Mao, H. Feick, H. Q. Yan, Y. Y. Wu, H. Kind, E. Weber, R. Russo and P. D. Yang, *Science*, 2001, **292**, 1897–1899.
43 L. Zhang, S. Bai, C. Su, Y. B. Zheng, Y. Qin, C. Xu and Z. L. Wang, *Adv. Funct. Mater.*, 2015, **25**, 5794–5798.
44 J. T. Li, Y. Lin, J. F. Lu, C. X. Xu, Y. Y. Wang, Z. L. Shi and J. Dai, *ACS Nano*, 2015, **9**, 6794–6800.
45 Z. L. Wang and J. H. Song, *Science*, 2006, **312**, 242–246.
46 M. R. Hasan, S. H. Baek, K. S. Seong, J. H. Kim and I. K. Park, *ACS Appl. Mater. Interfaces*, 2015, **7**, 5768–5774.
47 P. L. Wang, Y. M. Fu, B. W. Yu, Y. Y. Zhao, L. L. Xing and X. Y. Xue, *J. Mater. Chem. A*, 2015, **3**, 3529–3535.
48 H. P. Cong and S. H. Yu, *Adv. Funct. Mater.*, 2007, **17**, 1814–1820.
49 S. H. Ko, D. Lee, H. W. Kang, K. H. Nam, J. Y. Yeo, S. J. Hong and H. J. Sung, *Nano Lett.*, 2011, **11**, 666–671.
50 S. S. He, L. B. Long, X. Fang, G. Z. Duan, P. N. Chen, Z. T. Zhang and H. S. Peng, *J. Mater. Chem. A*, 2015, **3**, 9406–9410.
51 J. L. Yang, S. J. An, W. I. Park, G. C. Yi and W. Choi, *Adv. Mater.*, 2004, **16**, 1661–1664.
52 F. Lu, W. P. Cai and Y. G. Zhang, *Adv. Funct. Mater.*, 2008, **18**, 1047–1056.
53 A. B. Djurisic, X. Chen, Y. H. Leung and A. M. C. Ng, *J. Mater. Chem.*, 2012, **22**, 6526–6535.
54 M. Seol, H. Kim, Y. Tak and K. Yong, *Chem. Commun.*, 2010, **46**, 5521–5523.
55 J. Xu, X. Yang, H. Wang, X. Chen, C. Luan, Z. Xu, Z. Lu, V. A. L. Roy, W. Zhang and C. S. Lee, *Nano Lett.*, 2011, **11**, 4138–4143.
56 C. C. Li, K. L. Shuford, M. H. Chen, E. J. Lee and S. O. Cho, *ACS Nano*, 2008, **2**, 1760–1769.
57 Y. Yang, W. Guo, X. Q. Wang, Z. Z. Wang, J. J. Qi and Y. Zhang, *Nano Lett.*, 2012, **12**, 1919–1922.
58 S. M. Ansar, F. S. Ameer, W. F. Hu, S. L. Zou, C. U. Pittman Jr. and D. M. Zhang, *Nano Lett.*, 2013, **13**, 1226–1229.
59 Y. J. Fang, J. Sha, Z. L. Wang, Y. T. Wan, W. W. Xia and Y. W. Wang, *Appl. Phys. Lett.*, 2011, **98**, 033103.
60 V. Subramanian, E. Wolf and P. V. Kamat, *J. Phys. Chem. B*, 2003, **107**, 7479–7485.
61 X. M. Zhang, Y. Chen, R. S. Liu and D. P. Tsai, *Rep. Prog. Phys.*, 2013, **76**, 046401.
62 S. T. Kochuveedu, Y. H. Jang and D. H. Kim, *Chem. Soc. Rev.*, 2013, **42**, 8467–8493.

